Resolution Adapted Finite Element Modeling of Radio Frequency Interactions on Conductive Resonant Structures in MRI

Jürgen Ruoff,[1,2] Christian Würslin,[1,2] Hansjörg Graf,[1] and Fritz Schick[1]*

Prediction of interactions between the radiofrequency electromagnetic field in magnetic resonance scanners and electrically conductive material surrounded by tissue plays an increasing role for magnetic resonance safety. Testing of conductive implants or instruments is usually performed by standardized experimental setups and temperature measurements at distinct geometrical points, which cannot always reflect worst-case situations. A finite element method based on Matlab (The Mathworks, Natick, MA) and the finite element method program Comsol Multiphysics (Stockholm, Sweden) with a spatially highly variable mesh size solving Maxwell's full-wave equations was applied for a comprehensive simulation of the complete geometrical arrangement of typical birdcage radio-frequency coils loaded with small conductive structures in a homogenous medium. Conductive implants like rods of variable length and closed and open ring structures, partly exhibiting electromagnetic resonance behavior, were modeled and evaluated regarding the distribution of the B_1- and E-field, induced currents and specific absorption rates. Numerical simulations corresponded well with experiments using a spin-echo sequence for visualization of marked B_1-field inhomogeneities. Even resonance effects in conductive rods and open rings with suitable geometry were depicted accurately. The proposed method has high potential for complementation or even replacement of common experimental magnetic resonance compatibility measurements. **Magn Reson Med 000:000–000, 2011.** © 2011 Wiley-Liss, Inc.

Key words: magnetic resonance safety; heating; radio-frequency simulations; magnetic resonance compatibility of instruments; magnetic resonance compatibility of implants

A high and steadily increasing number of patients with conductive implants would benefit from magnetic resonance (MR) examinations, if hazardous interactions of the applied radiofrequency field and the implant could be excluded. Furthermore, minimally invasive interventional procedures can be navigated and monitored by MRI without X-ray exposure, but metallic and other conductive instruments are critical with respect to heating problems under radiofrequency (RF) irradiation.

MR safety of magnetic or electrically conductive devices is usually tested experimentally using American Society for Testing and Materials international standards, defining the setup and conditions for assessment of forces, torques, and heating caused by the MR scanner. Potential RF interactions are often evaluated by temperature measurements at distinct geometrical points around the conductive arrangement. Electromagnetic conditions of those experiments cannot really reflect a "worst-case scenario" under in vivo conditions, because the characteristics and transition impedance of the surrounding material are fixed, and points selected for temperature measurements are not always the most critical ones. Besides temperature measurements, analysis of artifacts in MR images can also help in revealing undesired RF interactions (1–4).

Up to now, only few situations have been tested or supported by numerical simulations for qualitative values of currents, specific absorption rates (SAR), electromagnetic field distribution, or even phase changes in the MR signals because of additional RF components from induced currents. Furthermore, especially in the human body electromagnetic parameters can differ in a wide range (5) depending on the geometry of the implant and the adjacent tissue types leading to a very complex situation for the desired "worst-case" consideration.

For cases with relatively long wavelengths compared with the dimensions of the RF coil, simulations have traditionally been based on circuit concepts invoking quasistatic field approximations (6–9). As B_0-fields and corresponding RF frequencies increase, these design concepts get inadequate, because currents in the coil elements do not behave according to results of circuit analysis: The wave behavior becomes more prominent, and the field distribution within the resonator may become nonuniform.

Full-wave electromagnetic analysis of RF coils in which the coil currents are assumed to be fixed to a specified value has been presented (10). However, at higher frequencies the coupling between the coil and the examined object increases significantly, resulting in additional disturbances of the electrical currents in the coil and the B_1-field distribution. This behavior renders the assumption of the fixed current values invalid. Modeling the correct current behavior is more difficult and requires significantly increased effort in structuring the simulation: Only an approach with minor simplifications combined with valid boundary conditions can address the related problems appropriately. By solving Maxwell's full-wave equations using suitable numerical techniques,

prediction of the field distribution becomes possible for given boundary conditions. Numerical approaches that have been used for this purpose comprise the finite difference time domain, the finite element method (FEM), and the method of moments, each of them having its individual advantages and drawbacks (11).

Former simulations have been performed using coarse regular geometrical grids with a constant mesh size across the entire simulation volume (12,13). Doing so implicates an enormous (or even impossible) computational effort for a suitable representation of very small conductive structures with curved surfaces (as implants) inside a large RF coil. In this work, a spatially highly variable mesh size has been applied for modeling the B_1- and E-field characteristics around and inside a typical birdcage RF coil at 1.5 and 3.0 T. Electromagnetic behavior of additional rod- or ring-shaped conductive structures inside the coil and the electromagnetic characteristics of the medium containing those structures can be considered as well. Time-dependent three-dimensional electromagnetic field distribution and currents in all conductive elements can be simulated by this new approach. The potential of predicting resonance behavior of implants depending on their geometry and material properties situated in homogenous medium is tested in this work. For each setup, numerical analyses were compared with experimental measurements to ensure the validity of the model.

MATERIALS AND METHODS

Coil Design

To obtain a realistic distribution of the RF magnetic field B_1 and its corresponding electrical field E, the most promising approach is to model the three-dimensional coil including all geometrical and electrical properties and apply the transmitter voltages at the feeding ports. Other approaches like an incident rotating magnetic field B_1 or reproducing the electromagnetic field of a coil with the help of several wave ports require knowledge about the exact field distribution at any place for every time step of the simulation.

Therefore, a band-pass-birdcage coil with an inner diameter of 32 cm and a length of 32 cm was considered for the following simulations (Fig. 1). The coil is constituted by eight equally distributed plane rungs and two plane end-rings with a width of 3 cm each. Because of the skin effect, electrical RF currents are pushed to the surface of the conductors, and it is therefore a valid simplification to describe all conductors of the coil as two-dimensional (perfect) electrical conductors (14). The boundary condition of the electrical field on a perfect electrical conductor is

$$\vec{n} \times \vec{E} = \vec{0} \qquad [1]$$

with $\vec{n}$ being normal vector of the surface and $\vec{E}$ the electric field vector (15,16). This means that the electrical field lines will always end orthogonally on the surface. The discrete impedances needed for tuning the resonance frequency of the band-pass-birdcage coil are equally distributed along the end-rings and the rungs.
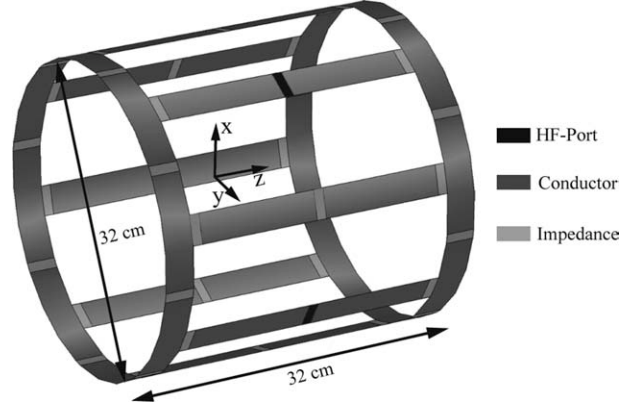

FIG. 1. Standard CAD-model of a quadrature driven birdcage coil consisting of conductor elements and impedances and two RF feeding ports. The z-axis is oriented along the outer magnetic field B_0.

The small resistive properties of real conductors can also be considered by these impedances. The transition boundary condition derived from Ref. 16 and used to describe these impedances and the RF feed (17) is

$$\eta \vec{\sigma} + \vec{n} \times ((\vec{E} - 2\vec{E}_0) \times \vec{n}) = \vec{0} \qquad [2]$$

In this equation, the incident electrical field $\vec{E}_0$ is given by $\vec{E}_0 = \vec{e}_h \frac{V}{h}$, where V is the transmitter voltage of the coil, and h is the height of the port with the unit vector $\vec{e}_h$ parallel to $\vec{E}_0$. The complex surface impedance η can be obtained from the desired impedance Z as $\eta = Z \cdot w/h$, where w is the width of the port. The total electrical field $\vec{E}$ and the surface current density $\vec{\sigma}$ are the resulting parameters.

The behavior of the electromagnetic field generated by this coil in air, the conductive structure, and in its surrounding medium can be described using Maxwell–Amperes law, Faradays law, and the material equations (18) by

$$\nabla^2 \vec{E} = \mu \kappa \frac{\partial \vec{E}}{\partial t} + \mu \varepsilon_c \frac{\partial^2 \vec{E}}{\partial^2 t}, \qquad [3]$$

with permeability μ, complex permittivity ε_c and conductivity κ.

At the transition between two domains with discontinuous material properties, according to Ref. 15, the boundary conditions

$$\begin{aligned} \vec{n} \times (\vec{E}_2 - \vec{E}_1) = \vec{0} \\ \vec{n} \times (\vec{H}_2 - \vec{H}_1) = \vec{\sigma} \end{aligned} \qquad [4]$$

have to be considered, where $\vec{\sigma}$ is the surface current on the electric conductor.

In a first attempt, the birdcage coil was excited at the center of two rungs, which are 90° apart from each other, by two sinusoidal RF signals shifted by 90° in phase (Fig. 1). The resistivity of the two RF feeding ports is 50 Ω. The inductivities, each consisting of mutual and self-inductance, are defined by the geometry and position of the conductors of the coil forming them. On the

basis of the former work about development of birdcage coils (19,20), the capacitors of the end-ring/rung branches of a band-pass-birdcage coil are found to be 75.4 pF/28.6 pF or 19.4 pF/6.8 pF to achieve a resonance frequency of 64 MHz (1.5 T) or 127 MHz (3 T), respectively. It should be mentioned that the BirgcageBuilder program (19) was used for determination of suitable capacities of the capacitors considering the above reported design of the birdcage coil. To achieve a better field homogeneity along the z-axis, the required capacity in each rung was split up into three discrete capacitors, which were distributed along the rung. To maintain the overall capacity of the rung, each of the three capacitors in this series connection must have three times the capacity of the overall capacity.

To obtain a uniform magnetic field with a flux density of 25 μT and a circular clockwise polarization with respect to the positive z-axis, the empty quadrature driven birdcage coil with this dimensioning has to be excited with an amplitude V_0 of 110 V at 1.5 T or 140 V at 3 T. In time transient analysis, the port voltage was defined as $V = V_0 \cdot \exp(j(2\pi ft + \varphi))$ with the phase angle φ. In time harmonic analysis, V_0 and φ could be used directly.

However, loading the birdcage coil (acting as a tuned oscillator) with samples creates additional inductances, which may cause a shift in resonance frequency or even corrupt resonance behavior. The intensity of the irregularities highly depends on the loading factor of the coil, the geometry and material properties of the sample, and the frequency used. For high loading factors at 3 T, the oscillating circuit can lose its resonance behavior. One possibility to get a highly uniform field distribution in this case is to adjust the values of all coil impedances for each sample individually to compensate additional inductances. In real MR coils, this can be done by matching and tuning elements.

A more robust approach is to increase the number of excitation ports feeding the coil (21). This kind of multi-port birdcage coil, where the RF input is supplied at the center of each rung (separated by 45° from each other) with a 45° phase shift, works similar to an antenna array. Using this type of excitation each rung acts as an antenna of its own and the quality of the field distribution no longer depends directly on the Q-factor of the coil. The impedances of the coil are mainly necessary to improve the uniformity of the current distribution along the conductors and have to be adapted for proper multiport excitation. In this configuration, the capacities of the impedances were set to 75.4 or 19.6 pF (at 1.5 and 3.0 T, respectively) at the end-rings and 25.16 or 6.55 pF, respectively, at the ends of each rung leading to resonance frequencies of 64 or 127 MHz, respectively. This setup generates a similar electromagnetic field distribution compared with the oscillating coil (Fig. 2). The transmitter voltage of each port was set to 110 and 140 V, respectively, and the input resistivity remained 50 Ω.

Mesh Generation and Numerical Analysis of Field Distribution

Numerical simulation was performed using Matlab (The Mathworks, Natick, MA) and the FEM-Program Comsol
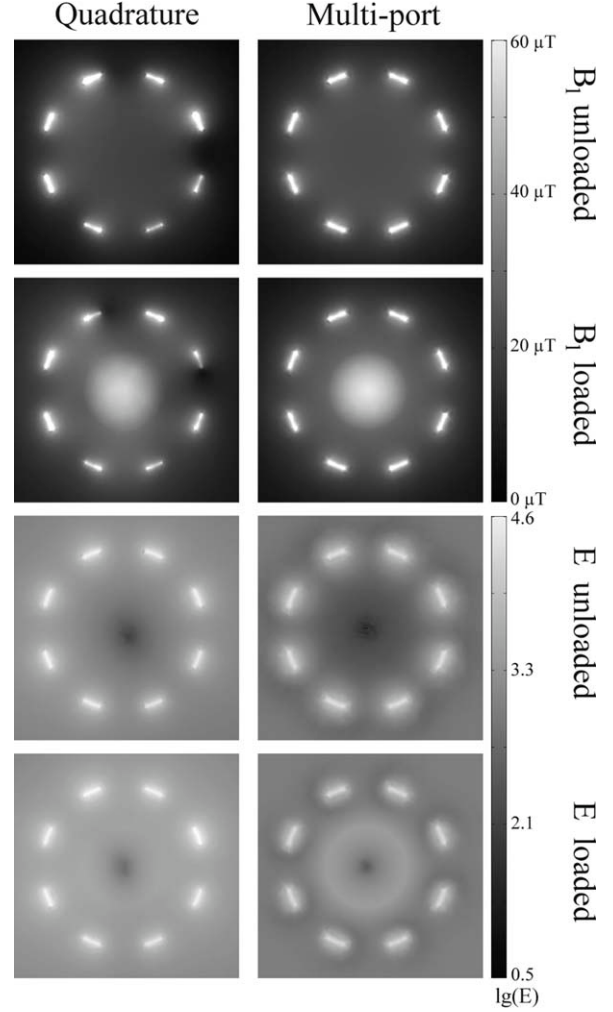

FIG. 2. Electrical and magnetic field distribution in a loaded and an unloaded quadrature and multiport driven birdcage coil at 127.74 MHz. In the loaded case, a cylindrical aqueous medium with a conductivity of κ = 0.0106 S/m was considered for a cylindrical volume with 20-cm length and 20-cm diameter centered in the coil.

Multiphysics (Stockholm, Sweden), whose meshing algorithm can generate meshes with variable element size and supports adaptive mesh refinement. For all surfaces and domains a maximum element size can be defined. Meshing errors might occur, if maximum element sizes of two adjoining domains differ too much. This problem was avoided by splitting domains into smaller subdomains and assigning different maximum element sizes to create a smoother transition. In this way, the investigated regions were meshed with up to 1.6 million spatially highly variable, nonuniform, unequally sized second-order tetrahedron elements with a minimum size of 25 μm. Doing so provided highly accurate modeling of small details and curved surfaces as shown in Fig. 3.

To model an infinite space while limiting the FEM computation space, the setup was enclosed by a spherical perfect matched layer according to Refs. 17 and 22. This perfect matched layer provided complete absorption and thus no reflection of electromagnetic waves.
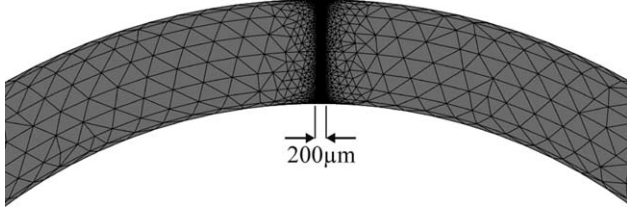
FIG. 3. Open ring structure with 0.2-mm gap width modeled with spatially highly variable mesh size.

To solve the resulting equation systems with up to 10 million degrees of freedom, a flexible generalized minimum residual method together with a geometric multigrid method for preconditioning was used (23). A relative tolerance of 10^{-6} was used as termination condition. The fine meshing in areas of steeply varying fields lead to convergent equation systems, which would not have been possible with a more coarse mesh. Computations were performed on a workstation with two 2.33 GHz Intel Xeon Quad Core E5345 and 32 GB of memory and took between 10 min and several hours.

Verification of Coil Model

As expected, the electromagnetic field distribution of the multiport birdcage coil was very similar to the field distribution of the standard unloaded oscillating birdcage coil (Fig. 2). However, the robustness of this field distribution to specimen induced distortions has been improved using multiple excitation ports according to Ref. 21. The numerically calculated field distributions in the unloaded birdcage coil using the standard (two port) and multiport version corresponded well with field distributions reported in the literature (21,24,25). The unloaded multiport birdcage coil, which was used for further simulations, showed B_1 variations of less than $\pm 1\%$ within a centered cylindrical volume of 10-cm length (along the z-axis) and 16-cm diameter.

Simulation of Conductive Rods Inside the Birdcage Coil

Many implants (e.g., hip prosthesis) and instruments (e.g., biopsy needles) contain conductive rod-like structures, which can act as $\lambda/2$ dipole antennas for the electrical field. The electromagnetic behavior of such structures is analyzed, particularly regarding the additional electrical field strength and currents. The wavelength of the electromagnetic field of a 3-T MR scanner is reduced from 2.35 m in air to ~ 0.26 m in mainly water containing tissue. Thus, rod-shaped structures with a length of about 13 cm are expected to get resonant in aqueous media. As the magnitude of the electrical field component is very low in the center of the RF coil and significantly stronger near the coil struts (i.e., in off-center position), the examined rod structures were shifted out of the isocenter. In both, simulations and experiments, cylindrical copper wire ($\kappa = 5.998 \times 10^7$ S/m, $\varepsilon_R \approx 1$, $\mu_R \approx 1$) with 4-mm diameter and lengths in between 6 and 18 cm were placed parallel to the z-axis with a 5 cm offset from the isocenter of the coil in negative y-direction.

Simulation of Conductive Rings Inside the Birdcage Coil

Open ring structures (as present in aneurysm clips or torus-like implants used in the spine) can act as magnetic antennas, if their orientation provides oscillating magnetic flux through the ring. In contrast to dipole antennas, magnetic antennas are mainly stimulated by the magnetic component of the electromagnetic field. For this reason, they are usually less influenced by their position inside the RF coil. The smaller the ring circumference (as compared with the wavelength λ), the more the magnetic component outweighs the electrical one. Antennas with a circumference of 0.3–0.1λ are so called electromagnetic antennas; the ones with a circumference below 0.1λ are called purely magnetic antennas. With suitable dimensioning even very small structures can get resonant. However, a decrease in antenna size is directly linked to a reduction of its efficiency. To compensate for the small radiation resistance, the Q-factor has to be high, leading to high voltages and currents. A worst-case scenario can be achieved by short, circularly looped wires, because they enclose the maximum area for a given wire length.

The ring structure represents a single-winding coil, whereas a gap in an open ring acts as a capacitor. Estimation of a suitable open ring geometry for resonant behavior at a given field strength B_0 was achieved by a simplified model: Together, structures of an open ring form a parallel resonant circuit which can be described using discrete circuit elements as shown in Fig. 4. Herein, R_L is the ohmic resistance of the ring, whereas G describes the conductivity of the gap. The resonance frequency of the circuit can be determined by setting the imaginary part of the ring's complex input impedance to zero (26), obtaining

$$\omega_0 = \sqrt{\frac{1}{LC} - \left(\frac{R_L}{L}\right)^2} \qquad [5]$$

The capacity C of the gap (treated as plate capacitor), the inductance L_{Ring} and the (RF)-resistance R_L of the ring can be approximated as

$$L_{Ring} = \mu \, r_R \left(\ln\left(\frac{8 \, r_R}{r_D}\right) - 2 \right) \qquad [6]$$

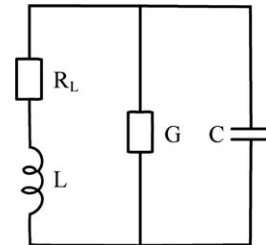$$R_L = \frac{r_R}{r_D} \sqrt{\frac{\mu \, \omega_0}{2 \, \kappa}} \qquad [7]$$

FIG. 4. Parallel resonance circuit as used for the characterization of open conductive ring structures.

$$C = \frac{\varepsilon \, \pi \, r_{\mathrm{D}}^2}{d} \qquad [8]$$

with loop radius r_{R}, wire radius r_{D}, permeability μ, and conductivity κ (26,27). The gap of the ring is represented by its width d and the permittivity ε of the fluid inside. The conductance of the gap G has no effect on the resonance frequency. However, it has a strong impact on the Q-factor (and thus the resonance step-up) and can be calculated by

$$G = \frac{\kappa \, \pi \, r_{\mathrm{D}}^2}{d}, \qquad [9]$$

On the basis of Eqs. 5–9, a copper wire wound to a ring requires a very small gap width to achieve a resonance frequency of 127 MHz (3 T), which—in an experimental setup—would be hard to realize. Therefore, all experiments and simulations for the magnetic antenna were performed at a magnetic field strength of 1.5 T. When using a copper wire with a radius of $r_{\mathrm{D}} = 2$ mm wound to a ring with a radius of $r_{\mathrm{R}} = 22.5$ mm, resonance behavior at a frequency of 64 MHz (1.5 T) can be expected for a gap width of $d = 0.13$ mm, according to Eqs. 5–9.

On the basis of these initial values from the simplified discrete model and based on Eq. 3, FEM eigenvalue calculations were performed to refine the necessary gap width for the desired eigenfrequency of the open ring structure. In contrast to the simplified model with discrete circuit elements, the FEM calculations account for side effects such as capacitor stray field, spatially extended dielectric, conductivity of the surrounding medium, and limited conductivity of the ring due to the skin effect. Those FEM eigenvalue calculations predicted a larger gap width of $d = 0.21$ mm for resonance at 64 MHz.

Experimental Procedures

Experiments were performed at 3.0 T for the rods and 1.5 T for the ring-like structures using single channel birdcage head coils with a wiring similar to the simulated one. Experiments on rods were carried out on a whole-body unit Magnetom Trio (Siemens Healthcare, Erlangen, Germany) operating at 3.0 T, whereas experiments on rings were performed on a whole-body 1.5 T Sonata system (Siemens Healthcare, Erlangen, Germany). The specimen (rods and closed and open rings) were positioned in a cylindrical perspex phantom with a size of $20 \times 20 \times 20$ cm^3, filled with the medium described in the next section. Positioning of the rods or rings inside the RF coil was according to the conditions used for FEM simulations.

In experimental MR compatibility tests, conductive structures are often surrounded by aqueous solution. Experimental test measurements were performed with a 1:200 solution of gadolinium in water. The properties of the medium were determined by measurement to a conductivity of $\kappa = 0.0106$ S/m, a relative permittivity of $\varepsilon_{\mathrm{R}} = 78$, and a permeability of $\mu_{\mathrm{R}} \approx 1$. These properties were used for the numerical simulations as well. Choosing a relatively low conductivity of the surrounding me-

dium resulted in pronounced resonance behavior of rods and open rings, supported by the low damping conditions. For comparison, simulations of the worst-case scenarios were also performed using a conductivity of $\kappa = 0.5$ S/m, which is matching conditions in the human body (5).

Several methods for B_1-mapping have been reported in the literature: "Double angle" (28) and "180 degrees signal null" (29) approaches lead to signal intensity variations, whereas techniques based on the Bloch-Siegert shift (30) work with a B_1-field-dependent signal phase. In our experiments, we aimed at a qualitative visualization of strong effects caused by the additional B_1-field generated by induced electrical currents in conductive rods and rings. Visualization of marked B_1-field variation near the conductive specimen, especially in cases of resonant coupling, was obtained by a standard 2D spin-echo sequence. This type of sequence has proven to be robust even in areas with very high B_1-field strengths (3), and provides distinct dark lines in areas with markedly increased B_1-field strength, where the excitation flip angle of the spin-echo sequence is $\sim 180°$ or multiples of $180°$. It was found in earlier experiments (3) that reduction of the nominal transmitter voltage by 50% leads to good visualization of slightly increased or decreased local B_1-fields in the surroundings of conductive materials. For this reason, experiments were carried out with halved transmitter voltage compared with the automatically adjusted value. Further measurement parameters were pulse repetition time = 500 ms, echo time = 15 ms, matrix size = 512×360, field of view = 256×180 mm^2, and slice thickness = 1.0 mm. In the surroundings of wires with strong induced currents, dark lines indicate at least fourfold increase of B_1 ($180°$ instead of $45°$ excitation flip angle in the spin-echo sequence or multiples of $180°$).

RESULTS

Analysis of Needle and Wire Model

Simulations of the magnetic flux density and MR images at 3 T for conductive rods with different lengths are exhibited in Fig. 5. As expected, the rise in magnetic flux above the value of the surrounding, homogenous field is most pronounced for a rod length of approximately half the wavelength λ (Fig. 5a). The simulation shows that the alternating current induced in the antenna increases the magnitude of the B_1-field close to the antenna to levels above 3 mT, which is 120 times the original field strength. In the MR images, several white–black–white transitions can be seen, when approaching the antenna. Dark lines occur when the excitation flip angle is raised to a multiple of $180°$, verifying the high local magnetic field enhancement in the vicinity of the antenna.

Maximum effects of the increased B_1-field can be found in the middle section of the resonant antennas with length near $\lambda/2$ (Fig. 5a), where the highest current density occurs (Fig. 5c). The maximum induced current at the center of the resonant antenna is 22.7 A. Areas of strong alternating electrical field and therefore high SAR occur at the ends of the antenna (Fig. 5b), where the
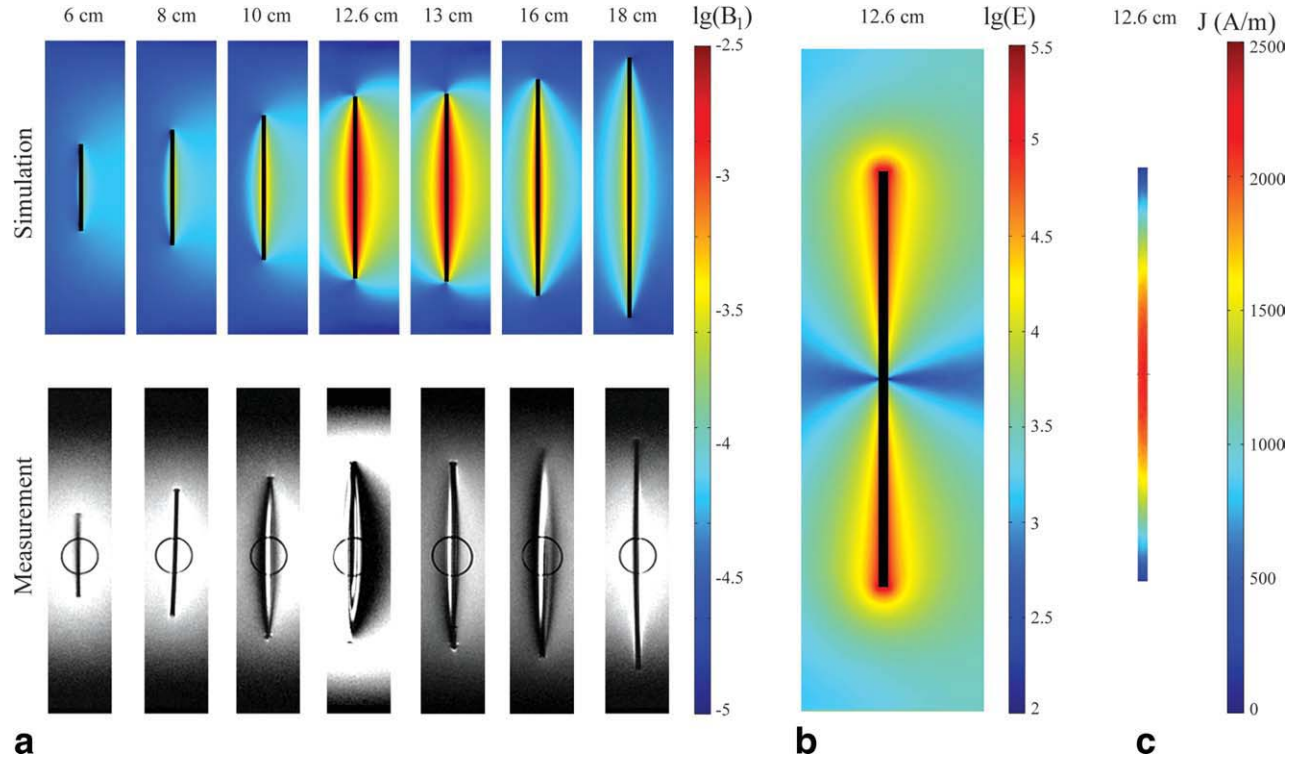
FIG. 5. a: Simulation of peak magnetic flux density B_1 in logarithmic scale and spin-echo magnitude measurements for different wire lengths. Parts of the mounting are visible in the MR images. b: Peak electrical field simulation in logarithmic scale for the 12.6-cm wire. c: Peak current density for the 12.6-cm wire. [Color figure can be viewed in the online issue, which is available at wileyonlinelibrary.com.]

electrical field locally raises up to 140 kV/m. This leads to a SAR of about 75 W/g in 1 cm^3 of the medium with a conductivity of 0.0106 S/m. For a higher conductivity of 0.5 S/m, which is more typical for human tissue (5), SAR drops to 18 W/g in the corresponding volume.

As the simulations show clearly increasing E-fields when moving from the center of the transmitter coil toward the outer areas, RF induced currents and potential heating in the vicinity of antennas also get stronger in this case.

Analysis of Ring Structures

MR images and simulations of the B_1-field in the surroundings of closed and open conductive rings with different gap widths are presented in Fig. 6. For minimizing the influence of the electrical field and achieving a homogenous excitation, the ring is positioned in the isocenter with sagittal orientation of the ring plane.

The closed ring (gap width of 0 mm) generates a small field enhancement outside the ring and shields the magnetic field on the inside, as predicted by Faraday's Law. For open conductive ring structures, the electromagnetic B_1-field induces a sinusoidal alternating electrical field inside the gap and a current along the ring. Effects on signal intensities in MR images are most significant, when the resonance frequency of the oscillating circuit nearly matches the frequency of the transmitted field. So, the ring structure with highest electrical field and current is the one with a resonance frequency close to the stimulating Larmor frequency, which was achieved

in our series of measurements for a gap of 0.2 mm. Simulations reveal an electrical field amplitude of 0.848 MV/m, which means an induced maximum voltage of 169.6 V at the gap. The peak eddy current on the ring is about 6.8 A, whereas about 0.143 A is reached in the gap medium. The electrical field distribution around the ring and the peak eddy current distribution are shown in Fig. 7. Average SAR (mean value integrated over one RF period) exposure of the medium in the gap was 5391 W/g. The dielectric heating of the ring structure and the gap can be calculated as

$$P_{\text{heat}} = \int_V \kappa \, \vec{E} \cdot \vec{E} \, dV \qquad [10]$$

and adds up to 24.45 W (gap only: 17.11 W) for the resonant ring with a 0.2-mm gap. Even higher dielectric losses could be achieved by varying the conductivity of the medium in the gap. A higher conductivity leads to higher dielectric losses but decreases the Q-factor and thus the eddy currents, whereas a low conductivity leads to a higher Q-factor and currents, but lower dielectric losses. A change of conductivity to 0.5 S/m leads to an altered resonance behavior with lowered resonance stepup. In our case, the SAR in the 0.2-mm gap of the resonant ring was reduced to 787 W/g. The exact temperature rise in the gap can hardly be measured, because the measurement equipment would influence the oscillating circuit and attenuate the resonance. So the simulation provides a unique tool for adequate predictions in those cases.
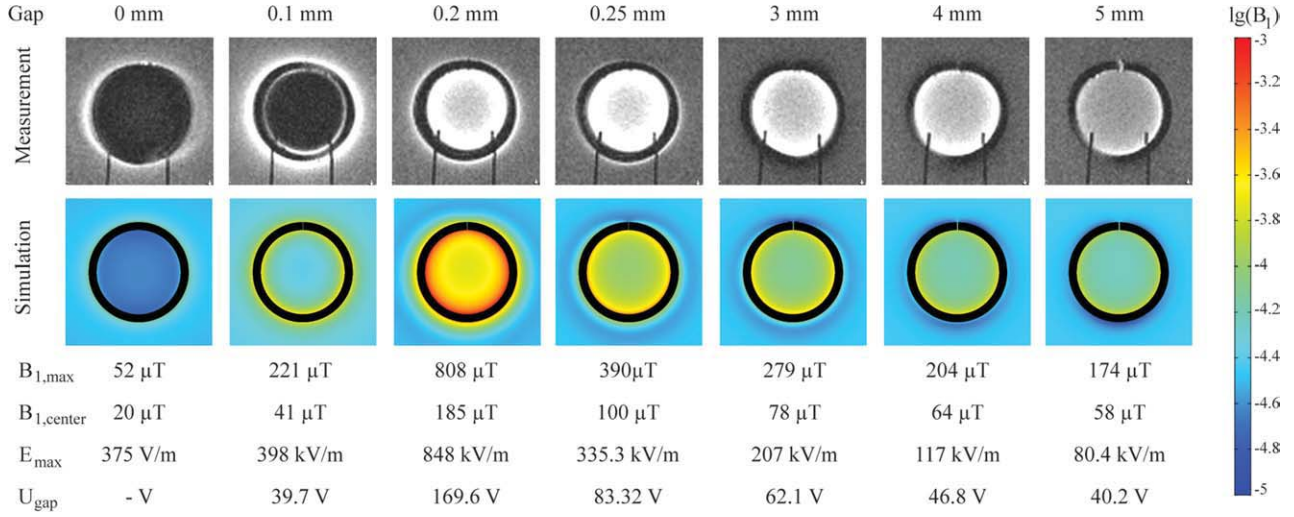
FIG. 6. Magnitude measurements and simulations of open ring structures with different gap widths. Parts of the mounting are visible in the MR images. The simulation shows the peak magnetic flux density B_1 in logarithmic scale. Maximum electrical field strength is present in the gap. Induced voltage over the gap is calculated.

The local B_1 phase shift caused by the eddy currents on the ring is shown in Fig. 8. From the time-dependent vector field, it is possible to calculate the phase shift between the outer B_1-field from the RF coil and the B_1-field components generated by the induced currents in the ring. In the given example, this phase shift amounts to ∼30°.

DISCUSSION

On the basis of their highly appreciated mechanical properties, metals often serve as materials for various implants and for instruments used during interventional procedures under MRI guidance. In most cases, the geometries of these instruments and implants are more complicated than the simple shapes of straight wires and rings (with and without gaps) presented here, however, the principles of RF interaction, resulting currents, and heating in surrounding media as well as artifacts in MR images can be well addressed using this simplified approach.

As shown in some of the examples in this work, conductive rods and open rings can get resonant and produce massive local electrical and magnetic field enhancements. These conditions might lead to strong electrical currents and high local SAR, which can produce heat and serious damage of tissue. In the case of electrical antennas, the conductive structure should have an extension of roughly half the wavelength of the stimulating field in the surrounding tissue. However, simulations and experiments showed that RF coupling must also be expected for rod lengths even with a deviation of several centimeters from $\lambda/2 = 12.6$ cm at 3 T. Electromagnetic or even pure magnetic antennas have no lower limitation on their size and have more degrees of freedom on their geometry. Even very small structures can get resonant in this way and produce serious field enhancements and related image artifacts.

RF amplitude and phase changes caused by the eddy currents can influence image formation. However, those visible effects are not always in accordance with local
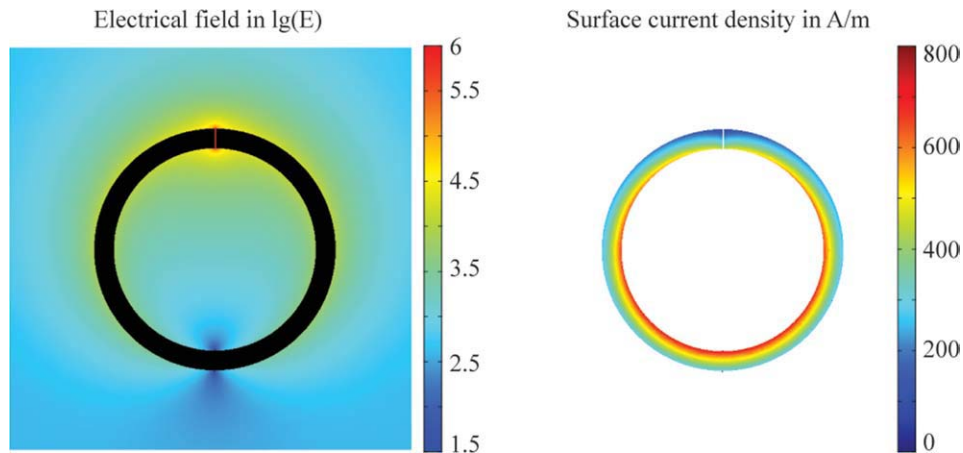

FIG. 7. Peak electrical field and current distribution of the resonant ring with 0.2-mm gap.
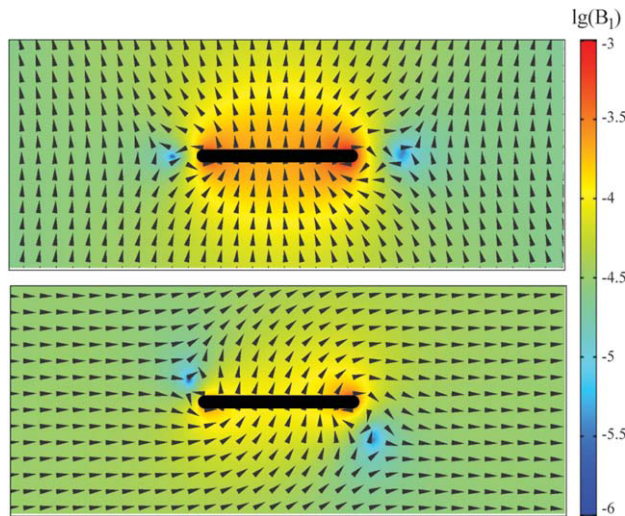
FIG. 8. Local phase change in coronal plane caused by the ring structure for a parallel and orthogonal B_1-field. The time-dependent effect on B_1 is visible as well. [Color figure can be viewed in the online issue, which is available at wileyonlinelibrary.com.]

heating, because imaging effects are usually dependent on RF magnetic fields superimposed to the transmitted RF, whereas heating depends mainly on local electrical fields and conductivity of tissues.

The mesh used for FEM simulations plays an important role for the quality of obtained results: In our examples with relatively thin rods and rings with submillimeter gaps, the system must be capable of resolving those details. Uniform meshes with cubic elements are not suitable for describing the exact geometry through their limited minimal size and shape (12). The new approach with nonuniform meshes as used for the simulations here is capable of modeling geometrical details as well as curved surfaces. On the other hand, variable mesh size saves computation time using large elements at regions of low electromagnetic variability and extremely small ones for a high precision at regions of higher interest. It is important for this kind of simulation that specimen details are modeled as exactly as possible to describe each possible influence on the electromagnetic behavior.

Comparison of simulations with adapted local mesh size with experimental results revealed very good correspondence. Simulations could predict the time transient electromagnetic field distribution precisely and can be used for calculations of SAR, B_1 and phase distributions. As the proposed simulation method allows for simulation of more complicated geometrical structures as tested in this work, a very powerful tool is offered for testing potential RF interactions of conductive implants or instruments at least inside homogenous media. In some cases, such simulations even seem to be the only way of testing, because other measurement procedures with probes would seriously influence the field distribution (as for example heat measurements in a narrow gap of a ring).

For an exact prediction of the behavior of implants or instruments under in vivo conditions, a more detailed model including correct electromagnetic characteristics of the tissues surrounding the conductive structures is required. On the basis of the FEM simulation approach with nonuniform meshes, series of simulations could be performed, taking into account possible tissue conditions surrounding a given metallic structure for more reliable worst-case calculations. Also liquid and heat transfer rates could be simulated for adequate calculation of temperature distributions during MRI. A coupled multiphysics system and the mathematical solving approach can be developed to improve analysis of the complex problem of conductive material in the body during MRI.

REFERENCES

1. Graf H, Lauer UA, Berger A, Schick F. RF artifacts caused by metallic implants or instruments which get more prominent at 3 T: an in vitro study. Magn Reson Imaging 2005;23:493–499.
2. Reinhardt J, Nguyen-Trong TH, Hähnel S, Bellemann ME, Heiland S. Magnetic resonance imaging of stents: quantitative in vitro examination at 3 Tesla. Med Phys 2009;19:278–287.
3. Lauer UA, Graf H, Berger A, Claussen CD, Schick F. Radio frequency versus susceptibility effects of small conductive implants—a systematic MRI study on aneurysm clips at 1.5 and 3 T. Magn Reson Imaging 2005;23:563–569.
4. Mattei E, Calcagnini G, Triventi M, Censi F, Bartolini P, Kainz W, Bassen H. MRI Induced Heating of Pacemaker Leads: Effect of Temperature Probe Positioning and Pacemaker Placement on Lead Tip Heating and Local SAR. In: Proceedings of the 28th IEEE EMBS Annual International Conference, New York City, USA; 2006.
5. Gabriel S, Lau RW, Corthout E, Gabriel C. The dielectric properties of biological tissues: I–III, Phys Med Biol 1996;41:2231–2293.
6. Amari S, Ulug AM, Bornemann J, van Zijl PCM, Barker PB. Multiple tuning of birdcage resonators. Magn Reson Med 1997;37:243–251.
7. Shen GX, Wu JF, Boada FE, Thulborn KR. Experimentally verified, theoretical design of dual-duned, low-pass birdcage radiofrequency resonators for magnetic resonance imaging and magnetic resonance spectroscopy of human brain at 3.0 Tesla. Magn Reson Med 1999;41:268–275.
8. Doty FD, Entzminger G Jr, Hauck CD, Staab JP. Practical aspects of birdcage coils. J Magn Reson 1999;138:144–154.
9. Rodriguez AO, Hidalgo SS, Rojas R, Barrios FA. Experimental development of a petal resonator surface coil. Magn Reson Imaging 2005;25:1027–1033.
10. Collins CM, Li S, Smith MB. SAR and B_1-Field distributions in a heterogeneous human head model within a birdcage coil. Magn Reson Med 1998;40:847–856.
11. Li BK, Liu F, Weber E, Crozier S. Hybrid numerical techniques for the modelling of radiofrequency coils in MRI. NMR Biomed 2009;22;937–951.
12. Bernardi P, Cavagnaro M, Pisa S, Piuzzi E. Safety Aspects of Magnetic Resonance Imaging for Pacemaker Holders. In: Proceedings of the International Conference on Electromagnetics in Advanced Applications (ICEAA), Torino, Italy; 2009. pp 869–872.
13. Mattei E, Calcagnini G, Censi F, Triventi M, Bartolini P. Numerical model for estimating RF induced heating on a pacemaker implant during MRI: experimental validation. IEEE Trans Biomed Eng 2010;57:2045–2052.
14. Giovannetti G, Francesconi R, Landini L, Santarelli MF, Positano V, Viti V, Benassi A. Conductor geometry and capacitor quality for performance optimization of low-frequency birdcage coils. Concepts Magn Reson Part B (Magn Reson Eng) 2004;20:9–16.
15. Jackson JD. Classical electrodynamics, 3rd ed. New York: John Wiley & Sons; 1998. pp 135–242.

16. Senior TBA, Volaki JL. Approximate boundary conditions in electromagnetics. London: The Institution of Electrical Engineers; 1995. pp 8–22.

17. Comsol AB. RF module user's guide, Version November 2008. Comsol 3.5a; 2008. pp 44–48, p 122, pp 146–147.

18. Chow T. Introduction to electromagnetic theory: a modern perspective. Sudbury: Jones & Bartlett Pub.; 2005. pp 353-354, pp 409–411.

19. Chin CL, Collins CM, Li S, Dardzinski BJ, Smith MB. BirdcageBuilder: design of specified-geometry birdcage coils with desired current pattern and resonant frequency. Magn Reson Eng 2002;15:156–163.

20. Renhart W, Wach P. Determination of capacitances in a twelve column MR-birdcage resonator using finite elements. IEEE Trans Magnet 2000;36:1910–1914.

21. Ibrahim TS, Lee R, Baertlein BA, Kangarlu A, Robitaille PM. Application of finite difference time domain method for the design of birdcage RF head coils using multi-port excitations. Magn Reson Imaging 2000;18:733–742.

22. Duan Y, Ibrahim TS, Peterson BS, Liu F, Kanfarlu A. Assessment of a PML boundary condition for simulating an MRI radio frequency coil. Int J Antennas Propag 2008, Article ID 563196, 10 pages, doi: 10.1155/2008/563196.

23. Saad Y. A flexible inner–outer preconditioned GMRES algorithm. SIAM J Sci Comput 1993;14:461–469.

24. Jin J, Chen J. On the SAR and field inhomogeneity of birdcage coils loaded with the human head. Magn Reson Med 1997;38:953–963.

25. Chen J, Feng Z, Jin J-M. Numerical simulation of SAR and B1-field inhomogeneity of shielded RF coils loaded with the human head. IEEE Trans Biomed Eng 1998;45:650–659.

26. Bird J (Hons), Electrocal and electonic principles and technology, 3rd ed. Burlington: Newnes; 2007. p 60, pp 247–253.

27. Paus CR. Inductance: loop and partial, 1st ed. Hoboken: John Wiley & Sons; 2010. pp 136.

28. Hornak JP, Szumowski J, Bryant RG. Magnetic field mapping. Magn Reson Med 1988;6:158–163.

29. Dowell NG, Tofts PS. Fast, accurate, and precise mapping of the RF field in vivo using the 180 degrees signal null. Magn Reson Med 2007;58:622–630.

30. Sacolick LI, Wiesinger F, Hancu I, Vogel MW. B_1-mapping by Bloch-Siegert shift. Magn Reson Med 2010;63:1315–1322.